

## Electronic Supplementary Information

### Supercurrent and multiple Andreev reflections in micrometer-long ballistic graphene Josephson junctions

Mengjian Zhu<sup>a,b\*</sup>, Moshe Ben Shalom<sup>a,c</sup>, Artem Mishchenko<sup>a,c</sup>, Vladimir Fal'ko<sup>a,c</sup>, Kostya Novoselov<sup>a,c</sup>, Andre Geim<sup>a,c</sup>

<sup>a</sup>*School of Physics and Astronomy, The University of Manchester, Manchester M13 9PL, UK*

<sup>b</sup>*College of Aerospace Science and Engineering, National University of Defense Technology, Changsha, Hunan, 410073, China*

<sup>c</sup>*National Graphene Institute, The University of Manchester, Manchester M13 9PL, UK*

#### 1. Device fabrications

Monolayer graphene was encapsulated between two relatively thick (typically, >30 nm) crystals of hexagonal boron nitride (hBN) by using the dry-peel transfer technique as detailed previously. The hBN-graphene-hBN stack was assembled on an oxidized Si wafer (300 nm of SiO<sub>2</sub>) and then annealed at 300 °C in a forming gas (Ar-H<sub>2</sub> mixture) for 3 hours. As the next step we used the standard electron-beam lithography to make a PMMA mask that would define contact regions. Reactive ion etching (Oxford Plasma Lab 100) was employed to make trenches in the heterostructure through the mask. The etching process was optimized to achieve high etching rates for hBN with respect to both PMMA and graphene. We used a mixture of CHF<sub>3</sub> and O<sub>2</sub> which allowed rates of 300, 60 and 3 nm per min for hBN, PMMA and graphene, respectively. Importantly, the PMMA mask was not cross-linked during the etching and allowed easy lift-off so that metal contacts could be deposited directly after plasma etching. This procedure allowed us to avoid additional processing and, accordingly, contamination of the exposed graphene edges. The same etching recipe was later used to define the device geometry. We chose that all Josephson junctions made on the same graphene crystal would have the same width  $W$ .

Due to the large difference in the etching rates of graphene and hBN, the resulting edge profile was found to exhibit a step of, typically, 5 nm in width as depicted schematically in Figure 1(a) of the main text. This step developed because graphene effectively served as a mask during etching of the bottom hBN, leading to a gradual exposure of graphene buried under the top hBN. In comparison with contacts prepared in the same manner but without the highly selective etching, the graphene nanostrip provided a notably lower contact resistance (see the section 5 for the discussion of the contact resistance).

For superconducting contacts, we used 50 nm thick films of Nb with an adhesion sublayer of Ta of 5 nm. Also, a few nm of Ta were put on top to protect Nb from oxidation. The tri-layer film was deposited by radio-frequency sputtering at a base pressure of  $\approx 10^{-9}$  Torr. We have no evidence about the damage effect from the RF sputtering to the 1D contacts. Instead, our results demonstrated high quality Josephson junctions with optimized contact resistance and enhanced interface transparency.

## 2. Characterization of superconducting contacts

As shown in Figure S1, the measured critical temperature of Nb electrode is  $T_c = 7.2$  K and the upper critical field  $H_{c2} = 3.5$  T (at  $T = 2$  K), which yield the superconducting energy gap  $\Delta = 1.76T_c \approx 1$  meV and the superconducting coherence length  $\xi = (\phi_0/2\pi H_{c2})^{1/2} \approx 10$  nm, respectively.

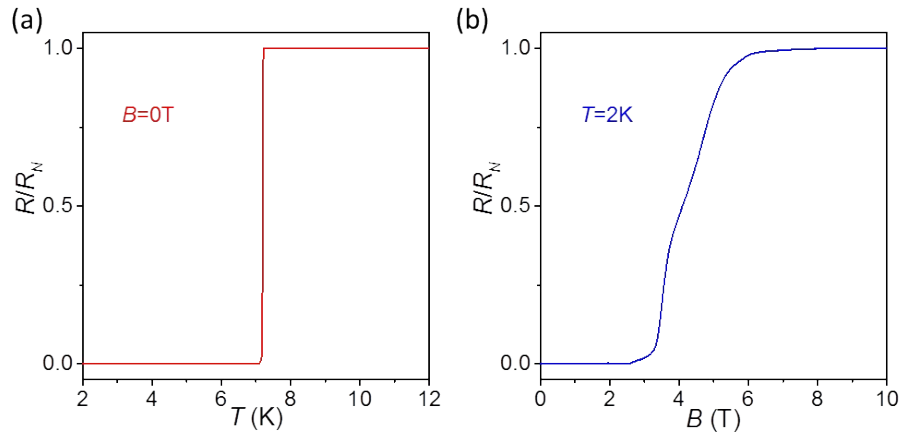


Figure S1. Characterization of superconducting contacts. (a) Normalized resistance of contacts as function of temperature at  $B=0$  T. (b) Normalized resistance of contacts as function of perpendicular magnetic field at  $T=2$  K.

## 3. Mobility of encapsulated graphene

In order to characterise the quality of our encapsulated graphene with edge contacts, we fabricate a Hall bar device on the same wafer with the Josephson junctions, see Figure S2.

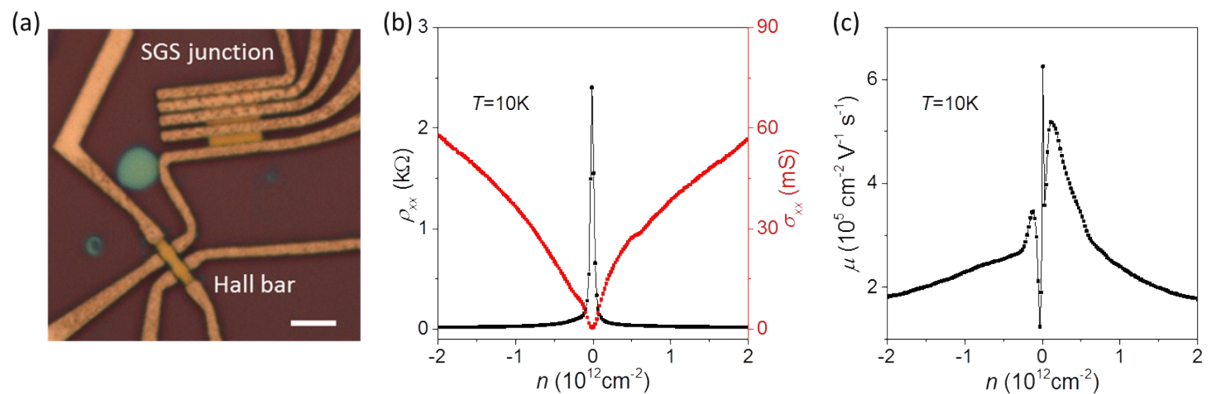


Figure S2. High mobility encapsulated graphene device with edge contacts. (a) Optical micrograph of graphene Hall bar and SGS junctions. The scale bar is  $5 \mu\text{m}$ . (b) Measured longitudinal resistivity  $\rho_{xx}$  (black) and conductivity  $\sigma_{xx}$  (red) as function of carrier density  $n$  of graphene Hall bar at  $T=10$  K. (c) Calculated field-effect mobility  $\mu$  at different  $n$ .

The field-effect mobility of graphene  $\mu$  is determined by the  $\sigma$ - $n$  measurement, as shown in Figure S2 (b). At small concentration the slope of  $\sigma$ - $n$  yields a mobility  $\mu \sim 300,000 \text{ cm}^2 \text{ V}^{-1} \text{ s}^{-1}$  at 10K. The value is in

agreement with the measured Hall mobility. For typical carrier density  $n \sim 10^{12} \text{ cm}^{-2}$ , such quality can be translated to an elastic mean free path for electron (hole) in graphene by:

$$L_e = (h/2e)\mu(\sqrt{n/\pi}), \quad (\text{s1})$$

where  $h$  is the Planck constant,  $e$  the elementary charge. In our graphene Hall bar device,  $L_e$  is about 3  $\mu\text{m}$ . For SGS junctions,  $L_e$  is larger than the longest junction length  $L=1.5 \mu\text{m}$  and therefore sufficient for causing ballistic transport conditions<sup>(1)</sup>.

#### 4. Measurements of Josephson junctions

All electrical transport measurements of our Josephson junctions were performed in a He-3 cryostat (Oxford Instruments) for temperature down to 0.3 K. The differential resistance was measured in a quasi-four-terminal configuration (two superconducting leads for driving current and the other two for measuring voltage drop) by combining a preamplifier with low-frequency lock-in technique ( $f=30 \text{ Hz}$ ). All electrical connections to our sample passed through a cold RC filter (cut-off frequency  $\approx 5 \text{ kHz}$ , Aivon Therma) placed close to the sample and an additional ac filter (cut-off frequency  $\approx 600 \text{ Hz}$ , home-made) was outside the cryostats. The excitation ac current used here was 2 nA.

#### 5. Ballistic transport and contact resistance in the normal state

The ballistic nature of our Josephson junctions in the normal state were proved by the observation of Fabry-Perot oscillations and the Sharvin resistance as well. For the 0.3  $\mu\text{m}$  junction, Fabry-Perot oscillations were clearly observed in negative back gate voltage regime, see the black curve in Figure S3(a). For the 1.5  $\mu\text{m}$  junction, due to higher frequencies, the oscillations almost smear in a large range of back gate voltage, as shown in main text Figure 1(a). However, if one zooms in Figure 1(a) in the main text, clear oscillations appear close to the Dirac point, as shown in the red curve in Figure S3(a). This is because when the carrier density is significantly low, the electrons have much longer fermi wavelength even comparable to the junction length.

For a ballistic graphene junction, the measured resistance is given by  $R_N = R_{Sh} + 2R_C$ , where  $R_N$  is the normal state resistance,  $R_{Sh}$  is the Sharvin resistance and  $R_C$  is the contact resistance per interface. The Sharvin resistance  $R_{Sh}$  can be expressed as  $h\pi/4e^2W\sqrt{2\pi n}$ , where  $W$  the junction width,  $n$  the carrier concentration and the number 4 comes from the spin and valley degeneracies of graphene. We plotted  $R_{Sh}$  using the Fermi wavelength  $\lambda_F$  that was calculated from carrier density  $n$  induced by gate voltage, using the standard equation  $\lambda_F = \sqrt{2\pi/C_g\Delta V_g}$  where the capacitance  $C_g \sim 5 \times 10^{10} \text{ cm}^{-2}/\text{V}$  was determined experimentally from the frequency of Shubnikov-Haas oscillations at high  $n$ , as shown in dashed blue curve in Figure S3 (b). One can see that, both the devices ( $L=0.3 \mu\text{m}$  and  $L=1.5 \mu\text{m}$ ) exhibit almost the same  $R_N$  vs.  $\Delta V_g$  curves not depending on the junction length, which means the resistance are only dominated by ballistic transport and contact resistance. Furthermore, both the devices see in Figure S3(b) exhibit the same shift in  $R_N$  upwards with respect to  $R_{Sh}$ , which indicates a constant resistance contribution,  $2R_C$ . For electron doping of graphene with  $\Delta V_g > 10 \text{ V}$ , which corresponds to  $n=5 \times 10^{11} \text{ cm}^{-2}$ ,  $R_{Sh} = 27 \Omega$  for our devices with  $W = 6 \mu\text{m}$  whereas we measured  $R_N = 38 \Omega$ . This yields  $R_C = 5.5 \Omega$  and contact resistivity of  $33 \Omega \cdot \mu\text{m}$ . We find the same  $R_C$  for all  $\Delta V_g > 10 \text{ V}$ . Thus, the quality of our graphene-

superconductor interface can also be characterized by their average transmission probability  $T_r$  given by  $T_r = R_{Sh}/(R_{Sh} + R_C)$ . For  $\Delta V_g > 10$  V, we calculate  $T_r = 0.83$ . That is, we have highly transparent graphene-superconductor interfaces.

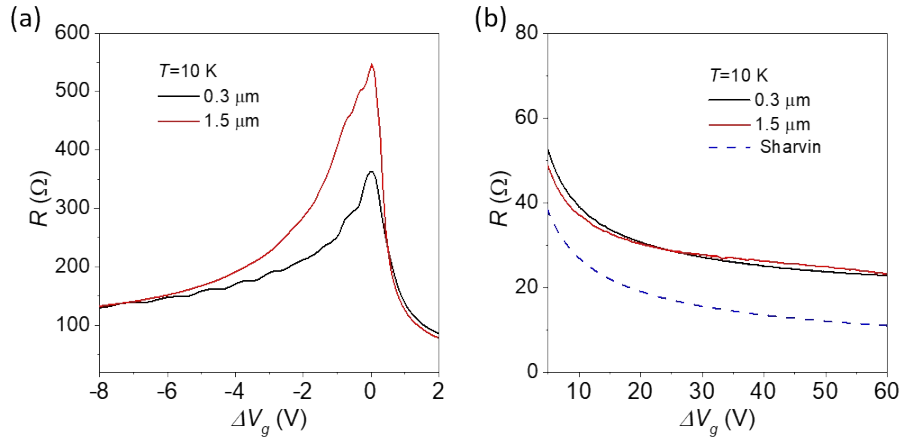


Figure S3. (a) The Fabry-perot oscillations in the hole regime and (b) Sharvin resistance in the electron regime of our 0.3  $\mu\text{m}$  (black) and 1.5  $\mu\text{m}$  (red) junctions. The dashed blue line in (b) is the calculated Sharvin resistance. The width of both two junctions is the same 6  $\mu\text{m}$ .

The observed multiple Andreev reflections (MAR) in superconducting state also allow an alternative estimate for the interface transparency  $T_r$  from the Blonder-Tinkham-Klapwijk model using the differential resistance at biases below  $\Delta$ . In the case of a single NS interface, it is known that the sub-gap resistance is half the  $R_N$  value if  $T_r = 1$  (perfect normal-electron transmission and only Andreev reflections at the interface). When a finite barrier strength  $Z$  is introduced, sub-gap  $dV/dI$  increases and can be calculated using this parameter all the way up to the tunnel limit ( $T_r = 0$ ). In the case of SNS junctions, calculations are more complicated and sensitive to employed models. This is particularly valid for wide ballistic junctions where gap-less Andreev spectrum has been predicted. It is nevertheless instructive to compare the observed MAR behavior with the simplest model. To this end, we focus on the sub-gap differential resistance at  $V_b < 0.3$  mV, significantly below  $\Delta/e$ , where individual Andreev resonances are no longer resolved. For 0.3  $\mu\text{m}$  junction in Figure S4(a) yields  $dV/dI \sim 0.5R_N$  for positive  $V_g$  (3 bottom curves), and  $dV/dI \sim 0.8R_N$  for negative  $V_g$ , (here  $R_N$  is determined as  $dV/dI$  at large biases  $V_b > 2\Delta/e$ , where its value reaches close to the normal-state resistance measured above  $T_C$ ). Repeating the previous analysis, we find  $Z \sim 0.5$  and  $0.8$ , which corresponds to  $T_r = 1/(1+Z^2) \sim 0.8$  and  $0.64$  for electron and hole doping, respectively. This is in good agreement with  $T_r = 0.83$  found from the normal-state contact resistance for electron doping. For 1.5  $\mu\text{m}$  junction, we were not able to observe MAR in electron regime and we could not determine  $T_r$  for electron doping. For hole doping, as shown in Figure S4 (b) using similar analysis, we find  $Z \sim 0.8$  and  $T_r = 1/(1+Z^2) \sim 0.6$ .

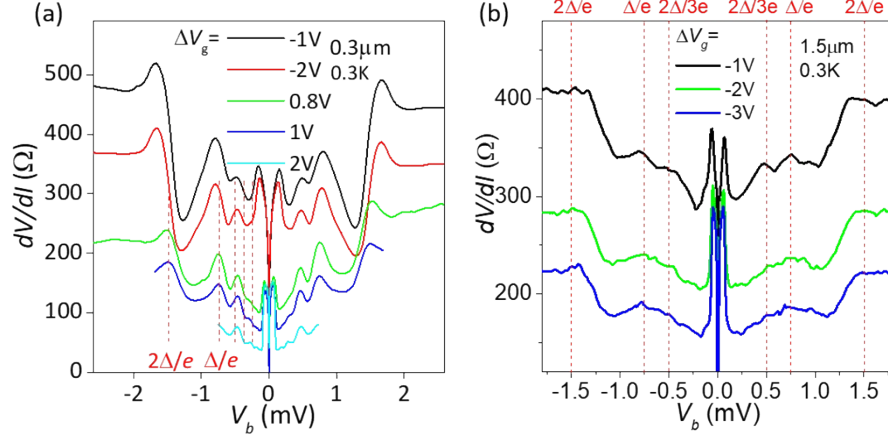


Figure S4. Multiple Andreev reflections in 0.3  $\mu\text{m}$  (a) and 1.5  $\mu\text{m}$  (b) long junctions. The MAR peaks are marked by dashed red lines and  $2\Delta/e$ .

### 5. Critical current of long ballistic SGS junctions

A long ballistic junction means the junction length  $L$  is smaller than the elastic mean free path  $L_e$  in graphene but larger than the induced superconducting coherence length in ballistic graphene  $\xi_b = \hbar v_F / \Delta$  ( $L_e > L > \xi_b$ ). Here,  $\Delta$  is the superconducting energy gap and  $v_F$  is the Fermi velocity in graphene. In our longest SGS junction case,  $L = 1.5 \mu\text{m}$ ,  $L_e \approx 3 \mu\text{m}$  and  $\xi_b \approx 0.5 \mu\text{m}$ , which implies that our longest junction is in the limit of long ballistic SGS junctions.

As an important figure of merit, the  $I_c R_N$  product of ballistic SGS junctions was theoretically predicted to be a constant of  $I_c R_N \approx 2.1\Delta/e$ , independent of doping and junction length.<sup>(2, 3)</sup> In main text Figure 3(b) gives the  $I_c R_N$  product as function of  $\Delta V_g$ . Away from CNP,  $I_c R_N$  product for each SGS junction holds a roughly constant value in both electron and hole doping regimes, independent of  $V_g$ . However, Figure 3(b) yields a coefficient of  $I_c R_N$  that is significantly smaller than the theoretical suggestions. For hole doping regime, the reduction can be attributed to the presence of p-n junctions. Even for electron doping regime with high  $T_r$ , we however obtain the maximum  $I_c R_N \approx 0.2\Delta/e$ , which is about ten times smaller than the theoretical predictions  $I_c R_N \approx 2.1\Delta/e$ . Considering the high quality graphene and transparent G-S interface in our SGS junctions, such reduction is unexpected.

Here, we propose a possible explanation for the unexpected small  $I_c R_N$ . The  $I_c R_N$  product of long ballistic SGS junction is still dominated by the Thouless energy,  $E_{th}$ . Despite the overall picture of Thouless energy in the ballistic system turns out to be more complex than the diffusive cases when considering physical quantities of a different nature. However,  $E_{th}$  remains the characteristic energy for various observables that still carrying the appealing significance of an inverse transport time through the system<sup>(4)</sup>. One can simply estimate  $E_{th}$  for our ballistic SGS junctions by quantum uncertainty principle  $E_{th} \tau \sim \hbar$ , where  $\tau = L/v_F$  is the carrier transport time through ballistic junction. Thus, we can obtain the Thouless energy:

$$E_c \sim \hbar v_F / L. \quad (s2)$$

For  $L=1.5\ \mu\text{m}$  ballistic SGS junction, the Thouless energy is  $E_{th} \approx 0.4\text{meV}$ , which is much smaller than the superconducting energy gap  $\Delta = 0.75\text{meV}$ . We can then aggressively assume that when  $E_{th} \ll \Delta$ ,  $I_c R_N$  product is limited by the Thouless energy rather than the superconducting energy gap. To experimentally check this assumption, we suggest a much shorter junction of  $L \ll \xi_b$  to approach  $E_{th} \gg \Delta$  regime, where  $I_c R_N$  product will be dominated only by  $\Delta$  and independent of  $L$ .

## 6. Temperature dependence of MAR

We measured the temperature dependence of MAR from 0.3 K to 8 K, as shown in Figure S5(a). We need to mention here that several works from other group and our group have shown that for Nb Josephson junction, the peaks instead of the dips in the  $dV/dI \sim V_b$  determine the  $2\Delta/ne$  due to the small coherence length in Nb, as we have discussed in the main text. If the dips are the signatures of MAR, as proposed by the referee, then the dip arounds 1 mV should correspond to  $2\Delta/e$  not  $\Delta/e$  because when  $V_b > 2\Delta/e$  the junction is biased to the normal state and the  $dV/dI$  is similar to the normal state resistance above  $T_C$ . Thus, we determined the MAR by the peaks in  $dV/dI$ . Furthermore, following the referee's suggestion, we extracted the  $2\Delta/e$  as a function of  $T/T_C$ , as plotted in Figure S5(b). As we can see that our experimental data fits the BCS calculation ( $2\Delta(T) = 2\Delta_0 \tanh\sqrt{1.74(T_C/T - 1)}$ ) very well. Worth to mention, we have measured more than 10 junctions with different length ranging from 0.2  $\mu\text{m}$  to 2  $\mu\text{m}$ , all the MARs behave very similar and can be well defined by the peaks of  $dV/dI$  instead of the dips.

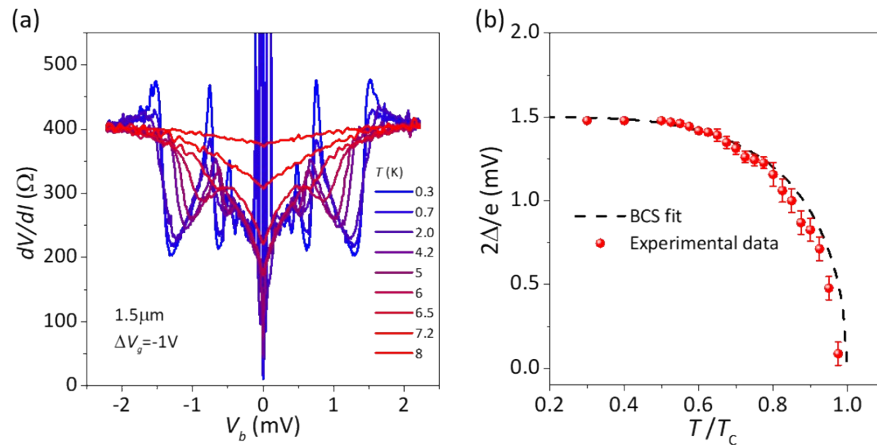


Figure S5. (a) Multiple Andreev reflections as a function of temperature. (b) Comparison between the extracted  $2\Delta/e$  as a function of  $T/T_C$  from the MARs and the calculated T-dependence of energy gap by BCS theory. The error bar is due to fitting.

## 7. Fraunhofer patterns of critical current at different doping levels

Figure S6 demonstrates another example of Fraunhofer patterns of critical current at different doping level. It's worth to mention here that our junction is in the wide regime, since the junction width  $W = 6\ \mu\text{m}$  is significantly larger than the length  $L = 1.5\ \mu\text{m}$  ( $W/L \gg 1$ ). Furthermore, our junction is also a long ballistic SGS junction. The junction length is smaller than the electron mean free path  $L_e$  ( $> 3\ \mu\text{m}$ ) but larger than the superconducting coherence length  $\xi_0 = \hbar v_F / \Delta_0 \sim 0.5\ \mu\text{m}$  ( $L_e > L > \xi_0$ ). For such geometry ballistic SGS junction, the  $I_c$  exhibits Fraunhofer-like oscillations as a function of the piercing magnetic flux

$\Phi$  with a period  $\phi_0 = h/2e$  and oscillation minima at integer multiples of the flux quantum  $\phi_0$ :  

$$I_c(B) = I_{c0} \left| \frac{\sin(\pi\Phi/\phi_0)}{\pi\Phi/\phi_0} \right|$$
, where  $B$  is the magnetic field and  $I_{c0}$  is the zero-field critical current (5). The  $I_c$  oscillations in wide and long ballistic graphene junctions have been shown in several experiments (6,7) and have been well described by theoretical calculations (8).

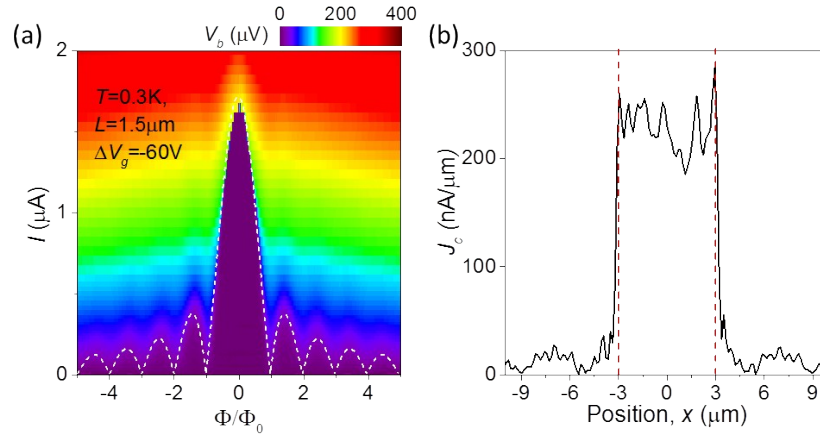


Figure S6. (a) Critical current as function of normalized magnetic flux ( $\Phi/\Phi_0$ ) at  $T=0.3K$  for  $\Delta V_g=-60V$ . Purple color is the zero voltage drop region, namely the superconducting state. The boundary of purple zone indicates the value of  $I_c$ . Dashed white curve corresponds to a calculation of a standard Fraunhofer pattern. (b) The supercurrent flow extracted from the experimental data using Fourier techniques is uniform through the entire SGS junction along the width direction. The red dashed lines define the junction width  $W=6\mu m$ .

## References

1. Mayorov AS, Gorbachev RV, Morozov SV, Britnell L, Jalil R, Ponomarenko LA, Blake P, Novoselov KS, Watanabe K, Taniguchi T, Geim AK. Micrometer-scale ballistic transport in encapsulated graphene at room temperature. *Nano letters*. 2011,11(6):2396-9.
2. Cuevas JC, Yeyati AL. Subharmonic gap structure in short ballistic graphene junctions. *Physical Review B*. 2006, 74(18):180501.
3. Titov M, Beenakker CW. Josephson effect in ballistic graphene. *Physical Review B*. 2006, 74(4):041401.
4. Altland A, Gefen Y, Montambaux G. What is the Thouless energy for ballistic systems?. *Physical review letters*. 1996, 76(7):1130.
5. Barzykin V, Zagoskin AM. Coherent transport and nonlocality in mesoscopic SNS junctions: anomalous magnetic interference patterns. *Superlattices and microstructures*. 1999, 25(5-6):797-807.
6. Shalom MB, Zhu MJ, Fal'ko VI, Mishchenko A, Kretinin AV, Novoselov KS, Woods CR, Watanabe K, Taniguchi T, Geim AK, Prance JR. Quantum oscillations of the critical current and high-field superconducting proximity in ballistic graphene. *Nature Physics*. 2016, 12(4):318-22.
7. Allen MT, Shtanko O, Fulga IC, Akhmerov AR, Watanabe K, Taniguchi T, Jarillo-Herrero P, Levitov LS, Yacoby A. Spatially resolved edge currents and guided-wave electronic states in graphene. *Nature Physics*. 2016, 12(2):128-33.
8. Rakyta P, Kormányos A, Cserti J. Magnetic field oscillations of the critical current in long ballistic graphene Josephson junctions. *Physical Review B*. 2016, 93(22):224510.

